

# Circulation Research

JOURNAL OF THE AMERICAN HEART ASSOCIATION

American Heart  
Association®   
*Learn and Live*<sup>SM</sup>

## Organization of Ventricular Fibrillation in the Human Heart

Kirsten H.W.J. Ten Tusscher, Rok Hren and Alexander V. Panfilov

*Circ. Res.* published online May 31, 2007;

DOI: 10.1161/CIRCRESAHA.107.150730

Circulation Research is published by the American Heart Association, 7272 Greenville Avenue, Dallas, TX 75214

Copyright © 2007 American Heart Association. All rights reserved. Print ISSN: 0009-7330. Online ISSN: 1524-4571

The online version of this article, along with updated information and services, is located on the World Wide Web at:

<http://circres.ahajournals.org>

Subscriptions: Information about subscribing to Circulation Research is online at  
<http://circres.ahajournals.org/subscriptions/>

Permissions: Permissions & Rights Desk, Lippincott Williams & Wilkins, a division of Wolters Kluwer Health, 351 West Camden Street, Baltimore, MD 21202-2436. Phone: 410-528-4050. Fax: 410-528-8550. E-mail:  
[journalpermissions@lww.com](mailto:journalpermissions@lww.com)

Reprints: Information about reprints can be found online at  
<http://www.lww.com/reprints>

# Organization of Ventricular Fibrillation in the Human Heart

Kirsten H.W.J. Ten Tusscher, Rok Hren, Alexander V. Panfilov

**Abstract**—Sudden cardiac death is a major cause of death in the industrialized world, claiming approximately 300 000 victims annually in the United States alone. In most cases, sudden cardiac death is caused by ventricular fibrillation (VF). Experimental studies in large animal hearts have shown that the uncoordinated contractions during VF are caused by large numbers of chaotically wandering reentrant waves of electrical activity. However, recent clinical data on VF in the human heart seem to suggest that human VF may have a markedly different organization. Here, we use a detailed model of the human ventricles, including a detailed description of cell electrophysiology, ventricular anatomy, and fiber direction anisotropy, to study the organization of human VF. We show that characteristics of our simulated VF are qualitatively similar to the clinical data. Furthermore, we find that human VF is driven by only approximately 10 reentrant sources and thus is much more organized than VF in animal hearts of comparable size, where VF is driven by approximately 50 sources. We investigate the influence of anisotropy ratio, tissue excitability, and restitution properties on the number of reentrant sources driving VF. We find that the number of rotors depends strongest on minimum action potential duration, a property that differs significantly between human and large animal hearts. Based on these findings, we suggest that the simpler spatial organization of human VF relative to VF in large animal hearts may be caused by differences in minimum action potential duration. Both the simpler spatial organization of human VF and its suggested cause may have important implications for treating and preventing this dangerous arrhythmia in humans. (*Circ Res.* 2007;100:0-0.)

**Key Words:** ventricular fibrillation ■ computer simulation ■ spatial organization

Ventricular fibrillation (VF) is the single most common cause of sudden cardiac death, the largest cause of death in the Western world. During VF, the contraction of the ventricles becomes rapid, uncoordinated, and highly ineffective, causing this condition to be lethal within minutes, unless halted by defibrillation. The highly disorganized contractions during VF are caused by a severely disturbed, turbulent conduction of the electrical excitation wave.

Experimental studies in animal hearts and tissue<sup>1-6</sup> have shown that the turbulent electrical activity typical of VF is caused by the presence of multiple reentrant waves of electrical excitation. Because of their reentrant behavior and high frequency, these rotors act as self-perpetuating, independent sources of excitation that take over control from the slower sinus node. The number of rotors present during VF is a good quantifier of the complexity and amount of disorganization of the excitation pattern. Results in animal hearts suggest that the number of reentrant sources present during VF increases as a function of heart size. For example, in rabbit hearts, VF can be driven by just 1 or 2 sources,<sup>2,7</sup> whereas in sheep hearts, VF is driven by 20 sources,<sup>4</sup> and in the larger pig and dog hearts the number of reentrant sources can be estimated at approximately 50.<sup>5,6</sup>

Studies of VF in the human heart are very limited, because of obvious practical and ethical constraints on clinical research. As a consequence, detailed data on the organization of human VF have for a long time been unavailable. The spatiotemporal complexity of VF may have important consequences for its treatment. For example, in modeling studies, it has been shown that minimum defibrillation energy decreases with decreasing wave pattern complexity.<sup>8,9</sup> It therefore remains an important question of whether human VF has a similar organization as VF in animal hearts of comparable size, such as the pig and dog hearts.

There were already some indications that human VF may be markedly different from VF in large animal hearts.<sup>10</sup> Clinically reported dominant frequencies of human VF lie at approximately  $5 \pm 1$  Hz,<sup>11-13</sup> which is approximately half that of the dominant frequency reported for VF in dog ( $10 \pm 2$  Hz<sup>5,14</sup>) and pig ( $10 \pm 1.5$  Hz<sup>14,15</sup>) hearts. Given that lower dominant frequencies correspond to longer rotor periods, longer activation pathways, and less complex excitation patterns,<sup>4,16,17</sup> this suggests a considerably simpler organization of human VF.<sup>10</sup>

Recently, several mappings of in vivo human VF were performed. Walcott et al<sup>18</sup> performed a small partial mapping

Original received February 15, 2007; revision received May 2, 2007; accepted May 23, 2007.

From the Department of Theoretical Biology (K.H.W.J.T.T., A.V.P.), Utrecht University, The Netherlands; and Institute of Mathematics (R.H.), Physics Mechanics, University of Ljubljana, Slovenia.

Correspondence to K.H.W.J. Ten Tusscher, Utrecht University, Department of Theoretical Biology, Padualaan 8, 3584 CH Utrecht, The Netherlands. E-mail khwjuss@hotmail.com

© 2007 American Heart Association, Inc.

*Circulation Research* is available at <http://circres.ahajournals.org>

DOI: 10.1161/CIRCRESAHA.107.150730

**Different Model Parameter Settings**

Parameter Setting	$G_{Na}$	$G_{Kr}$	$G_{Ks}$	$G_{pCa}$	$G_{pK}$	d Gate ( $V_{1/2}$ )	f Inactivation
Standard	14.838	0.172	0.441	0.8666	0.00219	-8	$\times 2$
Increased excitation	44.514	0.172	0.441	0.8666	0.00219	-8	$\times 2$
Steeper restitution slope	14.838	0.172	0.2205	1.8545	0.00073	-8	$\times 2$
Lower minimum APD	14.838	0.172	0.441	0.8666	0.00219	0	$\times 2$

Parameters that are not mentioned are kept unchanged from the default setting described in detail in table 1 of the report by Ten Tusscher and Panfilov.<sup>21</sup> Parameters that were varied were maximum conductance of the  $I_{Na}$ ,  $I_{Kr}$ ,  $I_{Ks}$ ,  $I_{pCa}$ , and  $I_{pK}$  currents (all in nS/pF) and the half activation voltage of the  $I_{CaL}$  d gate. An additional parameter that was used was the time constant for the f gate. Relative to the default setting, the time constant was multiplied by a factor for the voltage range  $V > 0$  mV, thus rescaling inactivation but not recovery kinetics.

of the left septal endocardium using a 36-pole catheter with 4-mm interelectrode spacing, and Nanthakumar<sup>12</sup> performed a partial mapping of the left ventricular epicardium using a 20 cm<sup>2</sup> plaque containing 504 electrodes with 2-mm interelectrode spacing. Nash et al<sup>13</sup> performed mappings of the complete epicardial surface during in vivo human VF using an elasticated sock containing 256 unipolar electrodes with 10-mm interelectrode distance to fit over the entire ventricles. Very recently, Masse et al<sup>19</sup> performed complete mappings of both endocardial and epicardial surfaces during human VF. For endocardial mappings an inflatable balloon catheter with an array of 112 bipolar electrodes was used for both ventricles, for epicardial mappings an elasticated sock with 112 bipolar electrodes was used. In all these studies, small numbers of large excitation waves repeatedly following the same pathways were reported, consistent with a simple organization of human VF. In addition, Nash et al<sup>13</sup> reported a small number of epicardial phase singularity points (PSs), suggesting the presence of only a small number of rotors underlying human VF.

A limitation of clinical and experimental measurements is that recordings can only be made on the surface of the heart, whereas the ventricles are 3D. Such a limitation does not apply to modeling studies, in which the complete 3D wave patterns can be studied. In this article, we use a detailed model of the human ventricles to study the 3D organization of human VF. Our model incorporates an electrophysiologically detailed model for human ventricular cells,<sup>20,21</sup> an anatomically detailed human ventricular geometry<sup>22</sup> and fiber direction anisotropy.

We compare characteristics of our simulated VF to the data from Nanthakumar et al<sup>12</sup> and Nash et al<sup>13</sup> and demonstrate a good agreement between simulated and clinical data in terms of ECG pattern, ECG frequency, surface wave patterns, and occurrence of epicardial reentry. We study the 3D organization of human VF and show that VF in the human heart is organized by as little as 10 reentrant sources present in the entire ventricular mass. Our results suggest that human VF indeed has a much simpler spatial organization than VF in pig and dog hearts.

We investigate the dependence of VF organization (number of rotors) on tissue anisotropy ratio, excitability, maximum action potential duration (APD) restitution slope and minimum APD. We find that the number of rotors depends strongest on minimum APD, with a difference in minimum APD of 77 versus 110 ms, leading to a 5-fold increase in rotor numbers. The other factors investigated, anisotropy, excit-

ability, and restitution slope, lead to maximally 2-fold increases in rotor numbers when varied within the physiological range. Interestingly, minimum APD differs substantially between humans and pigs and dogs.<sup>23-25</sup> Therefore, we hypothesize that it is the difference in minimum APD that causes the much simpler spatial organization of human VF.

**Materials and Methods****Human Ventricular Electrophysiology**

By omitting the discrete character of microscopic cardiac cell structure, the excitable behavior of cardiac tissue can be modeled as a continuous system using the following partial differential equation<sup>26</sup>:

$$(1) \quad C_m \frac{\partial V_m}{\partial t} = \frac{\partial}{\partial x_i} D_{ij} \frac{\partial}{\partial x_j} V_m - I_{ion}$$

$$(2) \quad I_{ion} = I_{Na} + I_{to} + I_{CaL} + I_{Kr} + I_{Ks} \\ + I_{K1} + I_{NaCa} + I_{NaK} + I_{pCa} + I_{pK} + I_{Na,b} + I_{Ca,b}$$

where  $C_m$  denotes the cellular capacitance,  $I_{ion}$  is the sum of the ionic transmembrane currents that together generate the action potential, and  $\partial \partial x_i D_{ij} \partial \partial x_j V_m$  represents the axial diffusive current flow between cardiac cells that leads to action potential propagation.  $D_{ij}$  is a 3D conductivity tensor describing the anisotropy of action potential propagation (see below, under Fiber Direction Field).

To represent the electrophysiological properties specific for human ventricular tissue, we use a detailed ionic model for human ventricular myocytes that describes the dynamics of the individual ionic currents and that is based on a large range of human electrophysiological data.<sup>20,21</sup> In the Table, we summarize the different parameter settings we used for our model. All parameters not mentioned in the Table are left unchanged from the default parameter setting of our model described previously.<sup>21</sup> Unless explicitly stated differently, we used the standard parameter setting of the Table.

**Human Ventricular Anatomy**

A 3D voxel description of human ventricular anatomy was obtained from an excised, structurally normal heart as described in detail by Hren.<sup>22</sup> In short, the heart was positioned as in the thorax and sliced in 1-mm-thick sections. The individual slices were digitized into 0.5-mm voxels. The data for the individual slices were stacked on top of one another to form a 3D voxel representation of the heart. Using interpolation techniques, a 0.25-mm voxel representation was derived from this 0.5-mm voxel model. The resulting model of the human ventricles consisted of approximately 13.5 million voxels.

**Fiber Direction Field**

Action potential propagation occurs faster in the direction parallel to the muscle fibers than in the direction perpendicular to the muscle fibers. To take this anisotropy into account, we needed a detailed description of the human ventricular myocardial fiber direction field. To obtain fiber orientation data for our human ventricular anatomy,

we used the following approach. We constructed a fiber orientation field from general knowledge on fiber architecture in the human heart,<sup>27</sup> combined with detailed data on the fiber architecture in the canine heart.<sup>28</sup> The rationale behind this is that it is known from classic studies on cardiac muscle fiber architecture that fiber architecture in the human and canine heart are very similar<sup>27,29</sup> and that the fiber orientation field in the dog heart has been studied in much more detail.

To construct our human ventricular fiber direction field, we first constructed principal surfaces that enclose the human ventricular myocardium and identified anatomical landmark points on these surfaces. Using surface data with these same anatomical landmarks for the canine geometry,<sup>28</sup> we then obtained a matching between the surfaces of the human and canine ventricles. This surface mapping then allowed us to assign canine fiber directions to the human ventricular surfaces. Intramural fiber direction was then derived from the surface fiber directions and general knowledge of intramural fiber rotation.<sup>27</sup> A full description of the construction method for the fiber direction field in our human ventricular anatomy is provided elsewhere.<sup>22</sup>

Recently, detailed data have become available for the fiber architecture of the human ventricles. We used these data to validate our fiber direction field. Winslow and coworkers used diffusion-tensor (DT)MRI<sup>30,31</sup> to derive fiber architecture in a single adult human heart and Jouk and coworkers used quantitative polarized light microscopy<sup>32,33</sup> to derive ventricular fiber architecture in young infants.

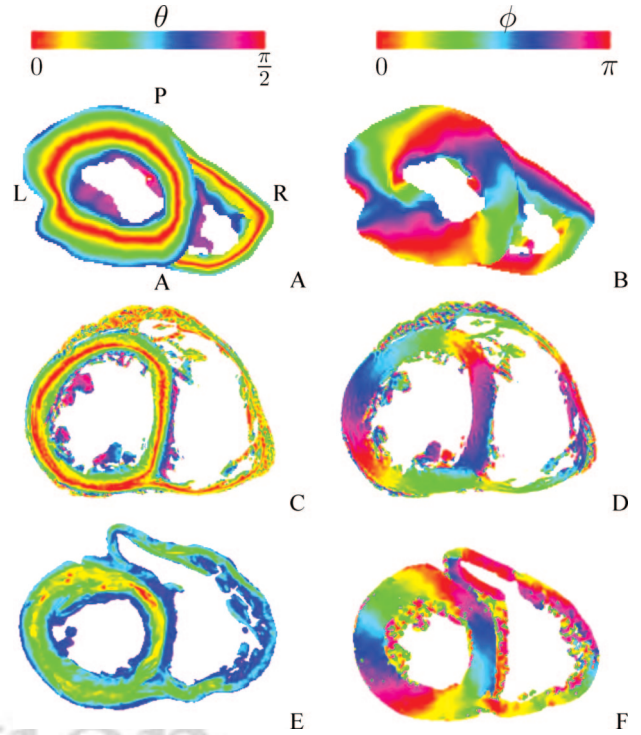
Figure 1 shows example cross-sections of the fiber direction field derived for our human ventricular geometry (Figure 1A and 1B) with the DTMRI data from Winslow and coworkers (Figure 1C and 1D)<sup>30,31</sup> and the light microscopy data from Jouk and coworkers (Figure 1E and 1F).<sup>32,33</sup> In our model, the elevation angle (Figure 1A) vary transmurally from approximately  $5\pi/8$  on the endocardium to 0 in the midwall, back to  $5\pi/8$  on the epicardium in both the left and right ventricle, reflecting transmural fiber rotation. A similar transmural change in elevation angle can be observed quite clearly in the left ventricle of the DTMRI data set of Winslow (Figure 1C) and somewhat less clearly in the right ventricle. In the light microscopy data from Jouk (Figure 1E), this transmural change in elevation angle is much less clearly present; the small angles found in the midwall in the other 2 data sets seem to be largely missing here. However, as stated by Jouk et al,<sup>33</sup> the polarized light microscopy method is not capable of resolving elevation angles close to 0. The absence of small midwall angles thus represents a limitation of their method rather than a difference among the 3 data sets.

Figure 1B shows the variation of the azimuth angle through the ventricular walls in our model. We see a clear circular to spiral shaped succession of different azimuth angles in the ring formed by the left ventricular free and septal wall, with the whole range of angles (colors) being visited twice. This variation in azimuth angles reflects the spiral shaped muscle structure of the heart. A less clear succession of azimuth angles with the whole range of angles being visited only once is present in the right ventricular wall. We can see a very similar variation in ventricular azimuth angles in the data sets by Winslow and coworkers (Figure 1D)<sup>30,31</sup> and Jouk and coworkers (Figure 1E).<sup>32,33</sup>

We carefully analyzed the complete datasets and found a similar correspondence between our model fiber field and the experimentally measured fiber fields of Winslow and coworkers<sup>30,31</sup> and Jouk and coworkers<sup>32,33</sup> for cross-sections taken at other positions or in different directions as for the cross-sections described above. We thus conclude that there is a good agreement between the fiber field we use in our model and the experimentally measured human ventricular fiber fields.

The derived and validated fiber direction field is used to derive the local conductivity tensor  $D_{ij}$  from the local fiber direction vector. Assuming that transverse conductivity is the same in all directions orthogonal to the direction of the muscle fiber axis, we described the ventricular conductivity tensor using the following equation:

$$(3) \quad D_{ij} = D_L \times \delta_{ij} + (D_L - D_T) \alpha_i \alpha_j$$



**Figure 1.** Comparison of muscle fiber direction field incorporated in our model (A and B), muscle fiber direction field obtained with DTMRI from an adult human heart<sup>30,31</sup> (C and D; data provided by P. A. Helm, R. L. Winslow, and E. R. McVeigh at <http://www.ccbm.jhu.edu/research/DTMRIDS.php>), and muscle fiber direction field obtained with quantitative polarized light microscopy<sup>32,33</sup> from a 24-week-old human infant heart (E and F; data provided by P. S. Jouk and Y. Usson). A, C, and E, Angle (elevation angle) that the fiber direction makes with the cross-section plane. B, D, and F, Angle (azimuth angle) that the fiber direction makes with the x-axis (horizontal to the right oriented axis). Cross-sections are taken at approximately the same level. Images are scaled to obtain similar sizes, and all have the same orientation. R indicates right ventricle; L, left ventricle; A, anterior; P, posterior.

where  $\alpha$  is the vector describing muscle fiber direction, and  $D_L$  and  $D_T$  are the conductivities in the longitudinal and transverse fiber directions, respectively. We use a ratio of 2:1 for the anisotropy of action potential conduction velocities, which is within the range of experimentally recorded ratios.<sup>34</sup> This results in a ratio of 4:1 for  $D_L$  to  $D_T$ . For  $D_L$ , we used 162 cm, which results in a longitudinal conduction velocity of approximately 70 cm/sec, consistent with experimental measurements.<sup>34</sup>

### Numerical Integration

We used a forward Euler scheme to integrate Eq. 3, using a time step of  $\Delta t = 0.02$  ms and a space step of  $\Delta x = 0.25$  mm. To integrate Eq. 3, we needed to evaluate at each point of the ventricular geometry the following Laplacian:

$$(4) \quad L(i, j, k) = \frac{\partial}{\partial x_i} D_{ij} \frac{\partial}{\partial x_j} V_m$$

This Laplacian can be discretized to the following equation:

$$(5) \quad L(i, j, k) = \sum_{l=0}^{18} w_l V_m(l)$$

where  $l$  is an index running over the 18 neighbors of the point  $(i, j, k)$  and the point itself, and  $w_l$  is the weight with which the voltage of a particular neighbor grid point contributes to the Laplacian of the

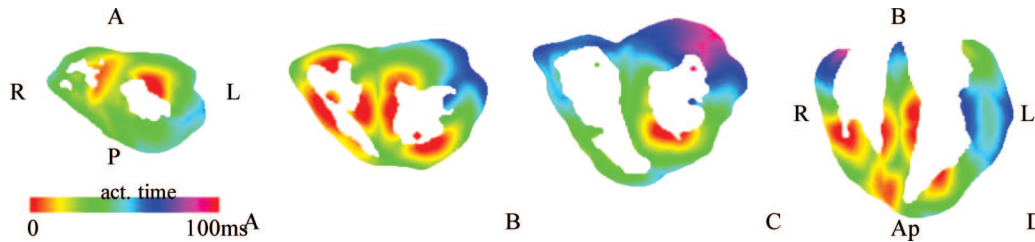


**Figure 2.** Activation times during the normal activation sequence in different ventricular cross-sections. Sections are taken at positions similar to the those shown in figures 1 and 2 in the report by Durrer et al.<sup>35</sup> R indicates right ventricle; L, left ventricle; A, anterior; P, posterior (orientations of cross-sections in A, B, and C are the same); B, basal; Ap, apical.

point  $(i, j, k)$ . The weights  $w_l$  were computed based on the local conductivity tensor  $D_{ij}$  and the local boundary situation in the point  $(i, j, k)$ : a neighbor  $l$  that lies outside the heart geometry receives a weight  $w_l=0$ . These weights were precomputed and stored as an efficient means to evaluate the Laplacian and automatically handle boundary conditions during the simulations.

### Normal Activation Sequence

Before using our model to study ventricular fibrillation, we first checked the validity of our model by simulating the normal activation sequence of the ventricles and comparing this with the classical data of Durrer et al.<sup>35</sup>

To simulate the normal ventricular activation sequence, we mimic activation by the Purkinje system by directly stimulating the endocardial sites of earliest activation as measured by Durrer.<sup>35</sup> Figure 2 shows activation time isochrones in different cross-sections of the ventricles. Positions of the cross-sections are chosen at similar locations as the cross-sections shown in figures 1 and 2 in the report by Durrer. Our simulated activation sequence shows a good agreement with the data from Durrer. Earliest activation occurs high on the left anterior paraseptal wall (Figure 2C), central on the left surface of the septum (Figure 2B and 2D), low on the left posterior paraseptal wall (Figure 2A), and on the low and central part of the right surface of the septum (Figure 2A and 2D). Latest activation occurs in the posterobasal part of the left ventricle (Figure 2C).

We find a total activation time of the ventricles of 95 ms, consistent with normal healthy QRS durations.

### Induction of Ventricular Fibrillation

Scroll waves were initiated using a S1-S2 stimulus protocol, with the S2 stimulus applied in the refractory tail of the S1 wave, leading to partial propagation block and spiral wave formation. Stimulus currents were applied at twice the diastolic threshold. We used different parameter settings of the electrophysiological model such that always an APD restitution slope considerably steeper than 1 was obtained (see the Table for the different parameter settings). Thus it was ensured that action potential alternans instability leading to spiral breakup and fibrillation like excitation dynamics would occur.

### Electrograms

Electrograms were obtained by assuming an infinite volume conductor and calculating the dipole source density of the membrane potential  $V_m$  in all voxel points of the ventricular myocardium, using the following equation<sup>36</sup>:

$$(6) \quad ECG = \int_V \frac{D \nabla V_m \vec{r}}{r^3} dV$$

where  $V$  is the domain of integration (ventricular volume), and  $r$  is the vector from each point in the tissue to the recording electrode. The recording electrode was placed 10 cm from the center of the ventricles in the transverse plane.

### Quantification of the Complexity of Wave Patterns: Number of Filaments and Phase Singularities

Quantifying the complexity of wave patterns arising during VF can be done by determining the number of rotors driving the excitation dynamics.<sup>2,6,37-41</sup> In the thick-walled ventricles, rotors are 3D scroll waves that rotate around a line of PSs called filaments. When such a filament intersects with the surface of the heart, a single PS occurs on the surface. In clinical and experimental studies, only detailed mappings of the surface of the heart can be performed. Therefore, only the number of epicardial (or endocardial) PSs can be determined. In simulation studies, both the number of filaments and the number of epicardial PSs can be determined.

Single voxels of scroll wave filaments were detected using an algorithm proposed by Fenton and Karma.<sup>42</sup> The algorithm finds the singular point of a 2D spiral wave by intersecting an isopotential line (in our case  $-60$  mV) with the  $dV/dt=0$  line. The algorithm was applied in all 3 directions. Intersection points thus found were stored as voxel data.

Individual filaments were detected by iteratively joining neighboring filament voxels and giving all voxels belonging to a single filament a unique identifier. To determine the number of epicardial PSs, scroll wave filaments were intersected with the epicardial surface. Filaments and PSs were determined at 10-ms intervals.

### Summarizing the Dynamics of Wave Patterns: Tracking Filaments in Time

A good way to concisely describe the dynamics of the complex VF wave patterns is by tracking filaments (or wavefronts) in time.<sup>37,39,40</sup>

The temporal dynamics of filaments can be summarized by a number of events: birth, the breakup of a scroll wave into multiple scroll waves; death, the disappearance of a scroll wave because it runs into a boundary or into unrecovered tissue; bifurcation, the splitting of a filament into 2 filaments; and amalgamation, the merging of 2 filaments into 1 filament as they bump into each other and merge.

We traced filaments in time by determining the overlap between filaments found at 2 consecutive time steps, similar to the approach followed in the report by Clayton and Holden.<sup>40</sup> If a filament present at time  $t+1$  does not overlap with any filament at time  $t$ , then a birth event has occurred. If a filament present at time  $t$  does not overlap with any filament at time  $t+1$ , then the filament has died. If a filament at time  $t$  overlaps with 2 filaments at time  $t+1$ , then a bifurcation has occurred. If 2 filaments at time  $t$  overlap with 1 filament at time  $t+1$ , then an amalgamation has occurred. Filaments at time  $t$  that overlap with 1 filament at time  $t+1$  simply continued.

If a new filament is born, it gets a unique new identity number. If a filament dies, this identity number is not reused. If a filament bifurcates into 2 filaments, the largest of the 2 new filaments keeps the identity number of the old filament; the smaller one gets a new number. If 2 filaments amalgamate into a single filament, the new single filament keeps the number of the longest existing of the 2 previous filaments.

We determined time of birth, death, bifurcation, and amalgamation, lifespan, and ultimate filament to which a filament can be

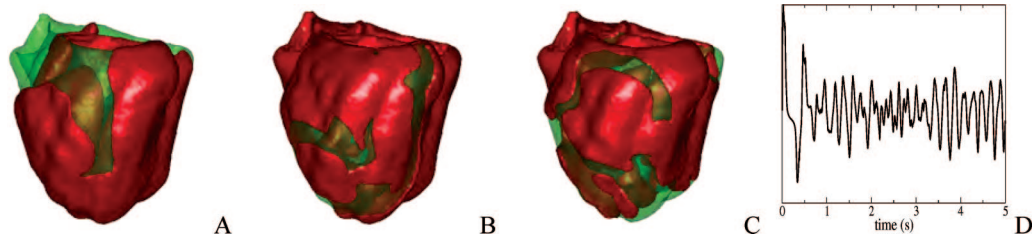


**Figure 3.** Ventricular fibrillation. In A, B, and C, red color indicates the excitation wave. A, Initial spiral wave pattern. B, Occurrence of the first wavebreak. C, Wave pattern arising after scroll wave fragmentation. D, Electrogram of the first 5 seconds of activity showing irregular VF-like dynamics.

traced back through bifurcation events, for all filaments. Because of the large total number of filaments ( $\approx 500$ ) and bifurcation and amalgamation events (500) during an entire episode of simulated VF, a directed graph displaying all filaments and all events becomes very tangled and hard to interpret. Therefore, we decided to plot for all filaments only their appearance (through either birth or bifurcation) and disappearance (through death or amalgamation) in time, without linking this to other filaments (in case they bifurcated from or amalgamated with another filament). Instead, we use different colors to display clusters of filaments that all descended from the same initial filament through bifurcation events. Ancestry trees showing the sequence of bifurcation events through which filaments have arisen are constructed for the largest filament clusters.

**Implementation**

All simulations were coded in C++ and MPI and were run on 20 processors of a Beowulf cluster consisting of 10 Dell 650 Precision Workstations (Dual Intel Xeon, 2.66 GHz). With this approach, simulating 1 second of wave propagation in the ventricles took approximately 12 hours of computational time. Ventricular geometry, wave patterns and scroll wave filaments were visualized using the marching cubes algorithm for isosurface detection in voxel data and OpenGL for isosurface rendering.

**Results**

**Ventricular Fibrillation**

We performed several simulations of VF by using a S1S2 protocol to initiate spiral waves in either the free wall of the left ventricle, the free wall of the right ventricle or the anterior wall of the ventricles. We used the standard parameter settings of our model (see the Table).

Figure 3 shows snapshots of consecutive wave patterns for the VF simulation in which a spiral wave was initiated in the left ventricle. Figure 3A shows the initial spiral wave pattern resulting from the S1S2 protocol. In Figure 3B, we show the occurrence of the first wave break shortly after the spiral wave was initialized. Figure 3C shows the wave pattern that has developed after 4 seconds. The ECG corresponding to these VF dynamics (Figure 3D) resembles clinically recorded ECGs of VF and has a dominant frequency of 4.8 Hz, similar to clinically reported frequencies.<sup>11–13</sup>

Before performing a full, 3D analysis of simulated human VF wave patterns, we first compared simulated VF surface wave patterns with clinically recorded surface wave patterns.

**Comparison With Clinical Data**

*Clinical Data of Nanthakumar et al*

Nanthakumar et al<sup>12</sup> were among the first to perform detailed mappings of wave patterns during in vivo human VF. They mapped epicardial activation patterns during 2-second intervals of VF in a 20 cm<sup>2</sup> area on the anterior and lateral free wall of the left ventricle, with a spatial resolution of 2 mm. Nanthakumar et al performed a detailed analysis of wavefront organization and dynamics. Their main conclusions were that human VF is characterized by the presence of large wavefronts that repeatedly follow the same pathways. In addition, they observed breakthrough, fractionation, and collision events and transient occurrences of reentry. To allow com-

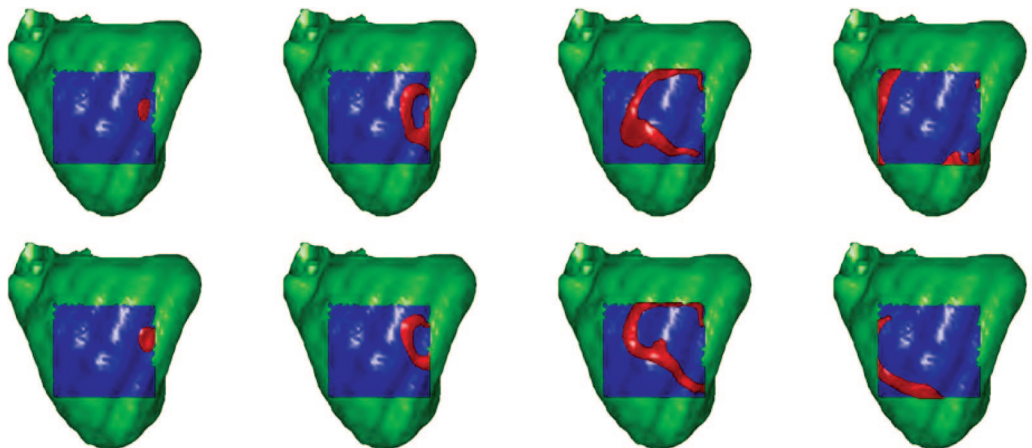


**Figure 4.** Reoccurring breakthrough pattern following the same propagation pathway and sweeping the entire recording area. Wavefronts are shown in red; the recording area is shown in blue. To demonstrate the repetitiveness of the propagation pattern, we show the sequence of breakthrough formation and propagation 2 times. In total, this pathway was repeated 5 times before a new wave pattern arose.

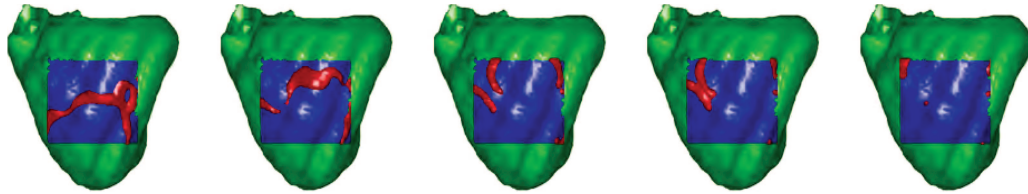


**Figure 5.** Fractionation and short-lived reentry pattern. Consecutive snapshots were taken at 2020, 2040, 2070, 2080, and 2100 ms. Snapshots show the fractionation of a single wavefront into 2 wavefronts, leading to the formation of 2 spiral waves that collide and annihilate each other.

parison between their clinical findings and our VF simulations, we analyzed our simulated wavefront patterns in an epicardial surface area of similar size and position.

In Figure 4, we show an example of a recurrent breakthrough pattern. A single breakthrough entered the recording area at the right producing a wavefront that sweeps the entire recording area. This propagation pattern repeated itself 5 times before changing into another wave pattern. The repeating breakthrough pattern indicates the temporary presence of an intramural scroll wave. This wave pattern is very similar to the breakthrough wave pattern shown in figure 3 of the report by Nanthakumar et al.<sup>12</sup>

Figure 5 shows an example of a wavefront fractionating into 2 separate wavefronts, leading to the formation of 2 spiral waves that subsequently collide and annihilate each other, similar to the sequence of breakup and collision events shown in figure 5, top 2 rows, in the report by Nanthakumar et al.<sup>12</sup> This figure shows that our simulated VF wave patterns are qualitatively similar to the wave pattern characteristics reported by Nanthakumar et al.

We also compared several quantitative characteristics of human VF reported by Nanthakumar et al with our simulation results. We found in our simulations that, on average, similar pathways were followed 7 times before wave patterns changed, close to the repeatability number of 8.3 reported by Nanthakumar et al. We observed reentry to be present 20% of the time, which is a factor of 2 to 3 higher than the value reported by Nanthakumar et al. However, this difference can be explained easily by the fact that their algorithm detects only reentry circuits completing at least 1 full cycle of reentry,<sup>38</sup> whereas we observed reentries completing as little as one-eighth part of a cycle. Furthermore, we observed reentries close to the edge of the recording area. Such reentries could not be detected by the algorithm used by Nanthakumar et al.<sup>12</sup> After correction for these differences,

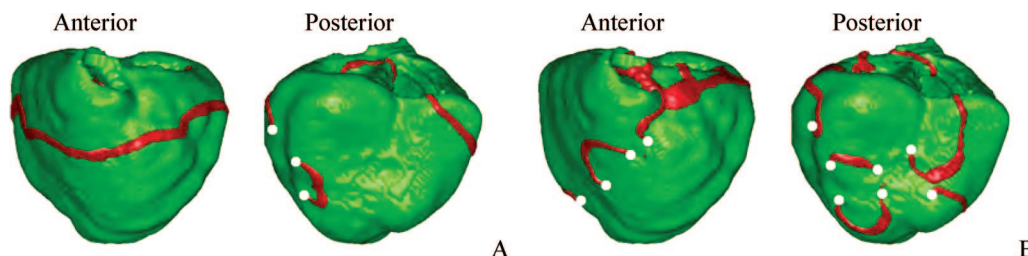
we observed similar frequencies of reentry occurrence as Nanthakumar et al.

#### *Clinical Data of Nash et al*

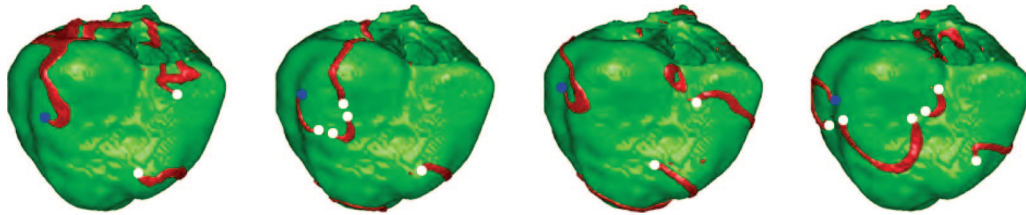
Recently, Nash et al<sup>13</sup> performed mappings of wave patterns during in vivo human VF on the entire ventricular epicardial surface, with a spatial resolution of 10 mm. They mapped VF activation patterns in a total of 10 patients in 20- to 40-second VF episodes and analyzed both wavefront and PS numbers and dynamics. Their main conclusions were that human VF is characterized by the presence of a few large coherent wavefronts and a small number of epicardial rotors. One or more epicardial rotors were present at all times during VF. To allow comparison between their findings and our simulation results, we analyzed our VF episodes in terms of epicardial wavefront patterns and PSs.

Figure 6 shows an example of the presence of both organized and less organized epicardial wave patterns during the same episode of simulated VF. Figure 6A shows a fairly organized wave pattern with only 3 epicardial PSs present occurring at 1680 ms after the onset of VF. Figure 6B shows a far less organized wave pattern with a total of 11 PSs occurring at 2720 ms after the onset of VF. A similar dynamical interchange of organized and less organized wave patterns can be seen in figure 7 of the report by Nash et al.<sup>13</sup>

Figure 7 shows an example of a persistent epicardial rotor that was present from 3940 until 5040 ms after the onset of VF. In the snapshots, we can also see the occurrence of wave breaks, leading to the presence of multiple much shorter-lived PSs. This wave pattern is also very similar to wave patterns observed by Nash et al (see figure 8A of Nash et al<sup>13</sup>). From these Figures, it follows that human VF is relatively organized and is characterized by a few large epicardial wavefronts and few PSs, with some PSs being present a longer period, whereas most PSs are very short lived. These findings



**Figure 6.** Presence of both organized and less-organized wavefront patterns during a single episode of VF. In red are the wavefronts; in white, the epicardial PSs. A, Anterior and posterior view of the epicardial wave pattern at 1680 ms after the onset of VF showing a relatively organized wave pattern with only 3 epicardial PSs. B, Anterior and posterior view of the epicardial wave pattern at 2720 ms after the onset of VF showing a much more disorganized wave pattern with a total of 11 PSs present.



**Figure 7.** Spiral wave persistence. In red are the wavefronts; in blue is the PS of the persistent spiral; in white, the PS of other spirals. Consecutive snapshots of the posterior epicardial wavefront pattern were taken at 3940, 4370, 4910, and 5020 ms showing the persistent presence of one of the spirals.

are qualitatively similar to the VF characteristics described by Nash et al.

For a quantitative comparison with the data from Nash et al, we computed the number of epicardial PSs. Figure 8A shows PS numbers as a function of time for the 3 episodes of simulated VF. In all 3 episodes, PS numbers increased during an initial transient of 1.5 second, and then fluctuated around an average of 8, 8, and 5 for initial spiral waves started in the left ventricle, right ventricle, or anterior of the ventricles, respectively. These numbers agree with the clinically reported numbers of epicardial PSs by Nash et al.<sup>13</sup> In Figure 8B, we show a histogram of the number of epicardial rotors present in each frame tallied over the 3 different VF simulations. Figure 8 shows that very low, but especially very high, numbers of PSs occur rarely and that PS numbers of approximately 5 to 7 occur most frequently, similar to what Nash et al reported (see figure 8C in the report by Nash et al<sup>13</sup>).

**Three-Dimensional Wave Patterns**

From the previous 2 sections, we conclude that our episodes of simulated VF closely resemble clinically recorded VF in terms of ECG pattern, ECG frequency, type and repeatability of surface wave patterns, and occurrence of epicardially observable reentries. In contrast to the clinical experiments, in our simulations we can also observe and analyze the full 3D ventricular wave patterns.

In Figure 9A, we show a snapshot of a full 3D wavefront pattern with 3D scroll wave filaments during simulated VF. The figure illustrates how a scroll wave with a transmural filament (o) gives rise to a single epicardial surface reentry, how a scroll wave with a U-shaped filament corresponds to

either 2 (\*) or 0 (#) epicardial PSs, and how a ring-shaped scroll wave filament (&) gives rise to 0 epicardial PSs. This demonstrates that not all 3D reentries (filaments) give rise to surface reentries (epicardial PSs) and hence how observing only (part of) the epicardial surface is likely to lead to an underestimation of the number of rotors driving VF.

Figure 9B shows the number of filaments as a function of time for 3 episodes of simulated VF. We see that after an initial transient filament, numbers fluctuate around an average of 12, 11, and 8 for initial spiral waves started in the left ventricle, right ventricle, or anterior of the ventricles, respectively. From a comparison with Figure 8A, it follows that the total number of rotors (number of filaments) is approximately a factor of 1.3 to 1.4 higher than the number of epicardially manifested rotors (epicardial PSs).

In addition to determining the number of rotors present at any given time point, we also determined the lifespan of individual rotors. Figure 10 shows filament lifespan histograms for 3 different VF simulations. We can see that for all 3 episodes of VF, many filaments (25%) have a lifespan of less than 50 ms, most filaments have lifespans between 50 and 200 ms (70%), and some filaments have lifespans between 200 and 1000 ms. Our filament lifespan distributions are very similar to the PS lifespan distributions reported by Kay et al<sup>37</sup> and distributions of the number of reentry cycles per reentry found by Valderrabano et al<sup>43</sup> and Rogers et al<sup>38</sup> (all in pig hearts), which also showed that most rotors are short lived and only a few rotors are present for a large part of the VF episode.

Finally, we analyzed how rotors were created and destroyed over time through birth, bifurcation, death, and

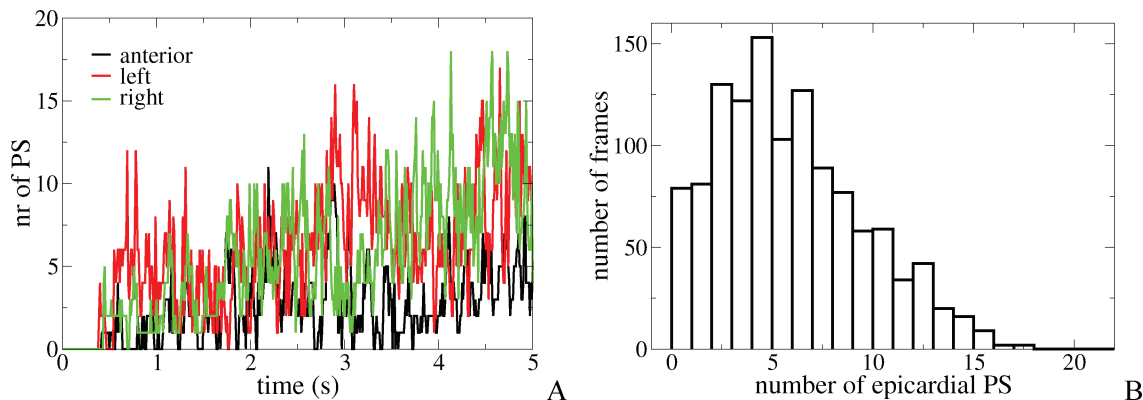


**Figure 8.** A, Number (nr) of epicardial PSs as a function of time for spiral waves initiated in the anterior wall (black), left free wall (red), and right free wall (green) of the ventricles. B, Histogram of the number of epicardial PSs present in each frame (snapshots taken at 10-ms intervals) tallied across 3 simulated VF episodes.

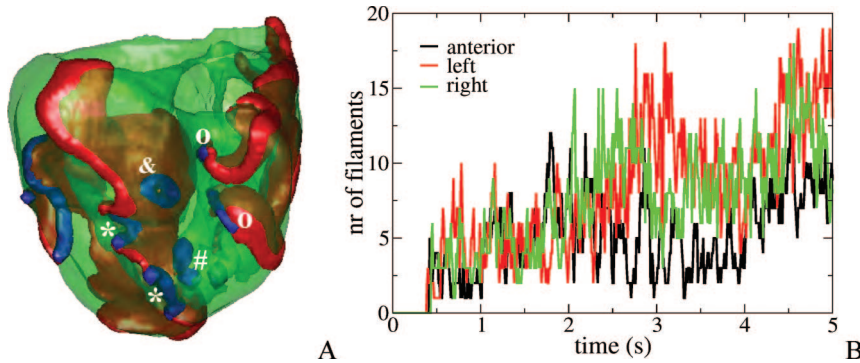


**Figure 9.** A, Complete 3D wavefront pattern (red) and scroll wave filaments (blue) during VF for a spiral wave initiated in the left ventricle. B, Number (nr) of filaments as a function of time for spiral waves initiated in the anterior wall (black), left free wall (red), and right free wall (green) of the ventricles.

amalgamation events for the entire episodes of simulated VF. Figure 11 shows the history of filaments present during 3 episodes of simulated VF. Horizontal lines indicate individual filaments. Lines start at the time a filament arises (through birth or bifurcation from another filament) and lines end at the time a filament disappears (through death or amalgamation with another filament). Short lines thus correspond to short-lived filaments and long lines correspond to long-lived filaments. New filaments get assigned a unique identity number (numbers are not reused once the old filament has disappeared). As a consequence, identity numbers of filaments being present at a certain time point increase over the course of time. With color, we indicate filaments belonging to the same cluster. We clustered filaments that descended through bifurcation from the same initial filament, ignoring clusters with less than 5 filaments. Filaments not belonging to a cluster (because they arose by birth rather than bifurcation) or belonging to a small cluster are drawn in black.

In Figure 11, we can see that over time, new filaments are steadily formed, whereas old filaments are continuously disappearing. From the figure, it is also clear that most filaments are present for only a short amount of time (many short lines), whereas only a few filaments are present during a large part of the episode (few long lines). We can also see that during VF, only a few larger filament clusters are present. In the 3 VF episodes, we found 10, 10, and 5 clusters, for the initial spiral started in the left, right, or anterior ventricle. These clusters accounted for 29%, 31%, and 22% of the total number of filaments, respectively. The largest cluster con-

tained 109, 63, and 58 filaments for these 3 VF episodes, representing 18%, 13%, and 15% of the total number of filaments. In the insets of Figure 11, we show the ancestry trees for the 1 or 2 largest filament clusters detected during the VF episode. The horizontal lines indicate all the filaments belonging to the same cluster, the vertical lines link a newly arising filament to an older filament it has just bifurcated from. We can clearly see that at the core of these large filament clusters is a single long lived scroll wave filament from which during its long lifespan numerous other filaments arise through bifurcation events.

For the episode of VF in which the initial spiral wave was started in the left ventricle, we detected a total of 609 filaments, 252 births, 331 deaths, 357 bifurcations, and 278 amalgamations. Adding birth and bifurcation events, a total of 609 events occurred in which new filaments were formed. Similarly, adding death and amalgamation events, a total of 609 events occurred in which filaments disappeared. For the other 2 episodes of VF, numbers of filaments and events were of similar magnitude. Total number of filament creation events was balanced by an equal number of filament destruction events for each of the three VF episodes. So, similar to the findings by Clayton and Holden,<sup>44</sup> our simulated VF dynamics are characterized by a finely tuned balance of rotor formation and destruction.

### Dependence of VF Organization on Conditions

Overall, we find that VF in the human heart is organized by a much smaller number of rotors than in animal hearts of

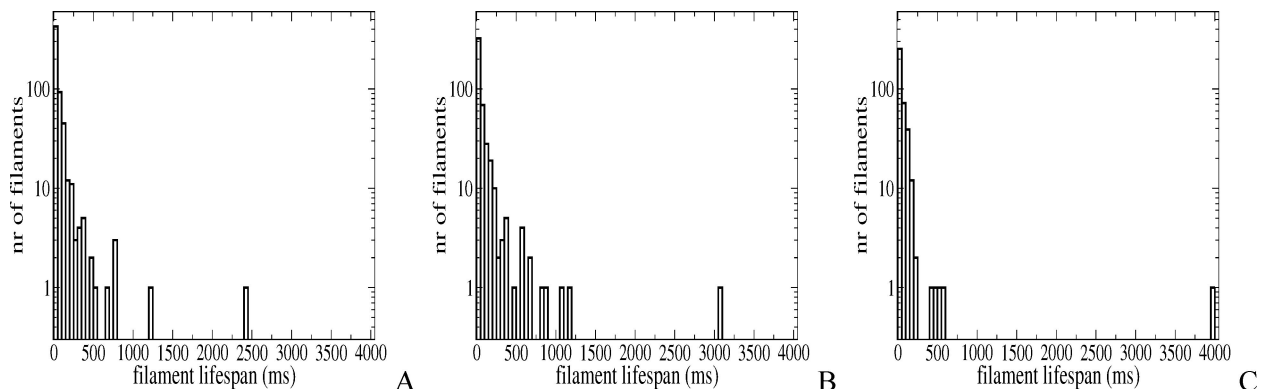


**Figure 10.** Filament lifespan histograms for 3 episodes of simulated VF. Note the logarithmic scale on the y-axis. A, Lifespan histogram for VF episode initiated with left ventricular spiral. B, Lifespan histogram for VF episode initiated with right ventricular spiral. C, Lifespan histogram for VF episode initiated with anterior ventricular spiral. nr indicates number.

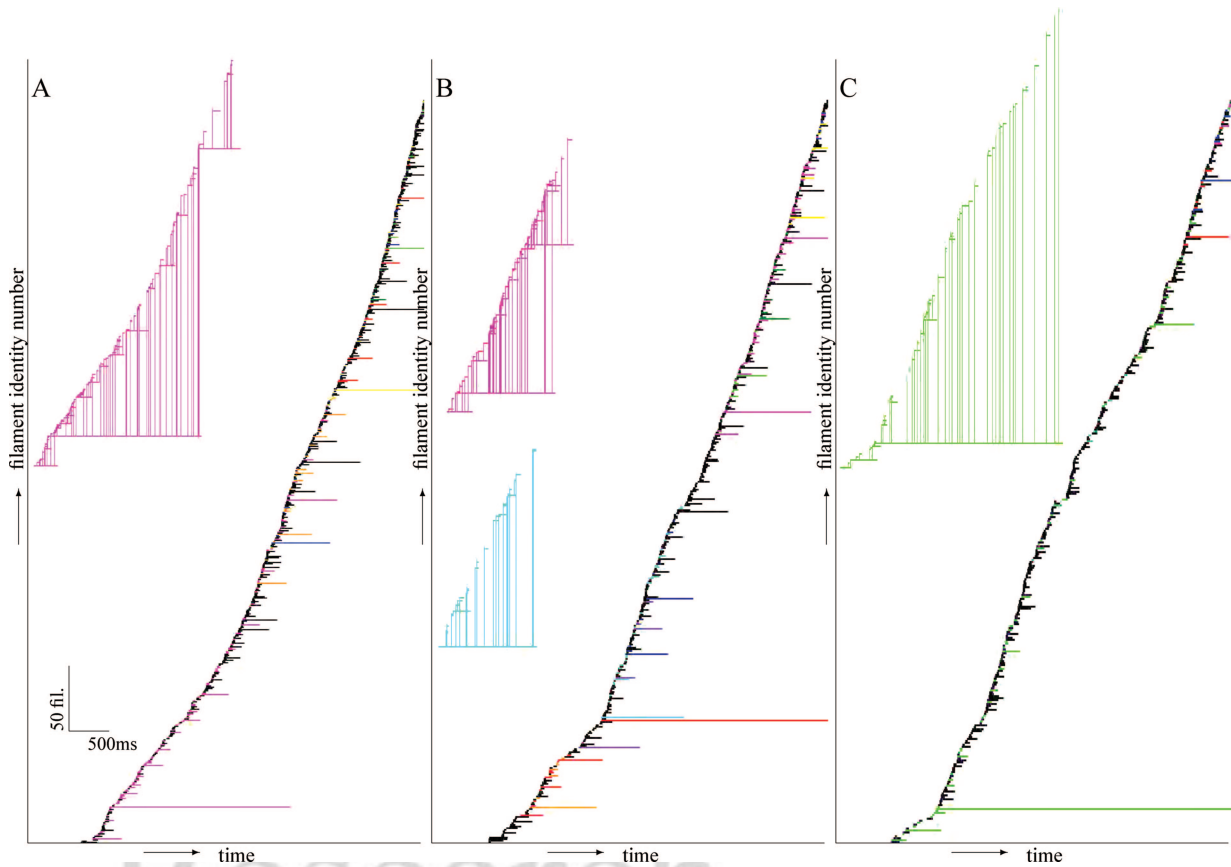


**Figure 11.** Filament history for the 3 episodes of simulated VF. A, For the VF episode initiated with left ventricular spiral. B, For the VF episode initiated with right ventricular spiral. C, For the VF episode initiated with anterior ventricular spiral. Horizontal lines correspond to individual filaments and start at the time a filament appears (through birth or bifurcation) and stop at the time a filament disappears (through death or amalgamation). Filaments are assigned unique identity numbers that are not reused once the old filament has died. Different colors are used to indicate clusters of filaments that can be traced back through bifurcation events to the same initial filament, which is the first filament of that color. We only use different colors for filaments with the same ancestor if the filament cluster has a size of 5 or more filaments. For all other filaments, which either have arisen through birth rather than bifurcation or belong to a very small cluster, we use the color black. As an inset, we show the ancestry tree of the largest (or 2 largest) filament clusters, in which vertical lines are used to show from which filament new filaments bifurcated.

comparable size. An important question thus is which factors determine the number of rotors driving VF. To answer this question, we investigated the influence of tissue anisotropy, excitability, maximum APD restitution slope, and minimum APD on the number of reentries present during VF.

### Dependence on Anisotropy Ratio

Thus far, we assumed an anisotropy ratio of 1:4 between transversal and longitudinal conductivity.

However, reported ratios between longitudinal and transversal conduction velocities vary. Here we performed simulations with anisotropy ratios of 1:2, 1:4, and 1:7 to study the influence of anisotropy on the complexity of wave patterns during VF. Model parameter settings were the same as in the previous sections. Spiral waves were initiated in the left ventricle.

For all anisotropy ratios, spiral breakup and subsequent fibrillation-like dynamics occurred. Figure 12A through 12C shows snapshots of wave patterns during VF, and Figure 12D through 12F shows snapshots of the scroll wave filaments driving VF for the different anisotropy ratios. We can see that the complexity of the wave patterns and the number of filaments driving VF increase with increasing anisotropy ratio.

In Figure 13A and 3C, we show the number of filaments and PSs as a function of time for the different anisotropy ratios. We see that after an initial transient, average filament numbers approach 5, 12, and 16, and average PS numbers approach 4, 8, and 12 for anisotropy ratios 1:2, 1:4, 1:7, respectively. In all 3 cases, ratios between total number of rotors (filaments) and epicardially manifested rotors (PSs) were around 1.3 to 1.4.

An increase in anisotropy ratio effectively increases ventricular volume. In Figure 13B and 13D, we show the number of filaments and PSs for the different anisotropy ratios normalized relative to the effective ventricular volume resulting from the 1:4 anisotropy ratio. We see very similar normalized filament and PS numbers, indicating that the increase in number of reentrant sources driving VF as anisotropy ratio increases is entirely caused by an increase in effective tissue volume.

### Dependence on Excitability

Another factor that may be subject to some variation is tissue excitability. We investigated the effect of excitability on wave pattern complexity during VF by increasing the maximum conductance of the fast sodium current.

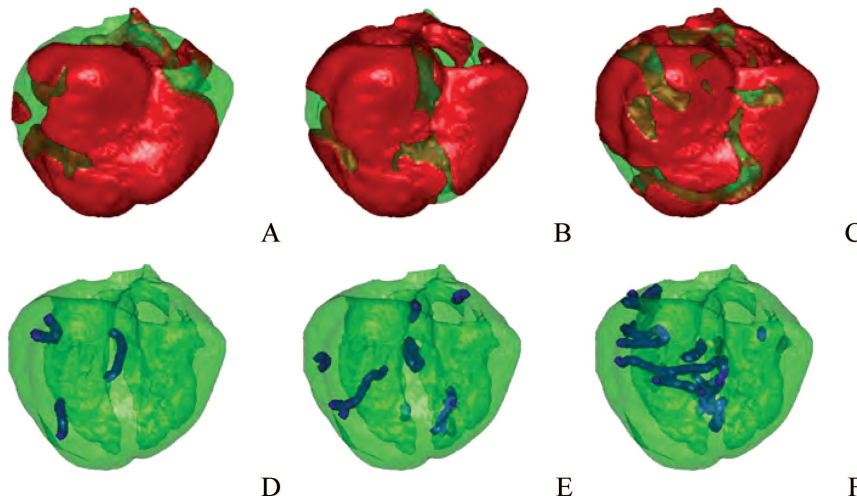


**Figure 12.** Effect of anisotropy ratio. Snapshots of excitation wave patterns (red) and scroll wave filaments (blue) arising after spiral breakup for 3 different anisotropy ratios: 1:2 (A and D), 1:4 (B and E), and 1:7 (C and F).

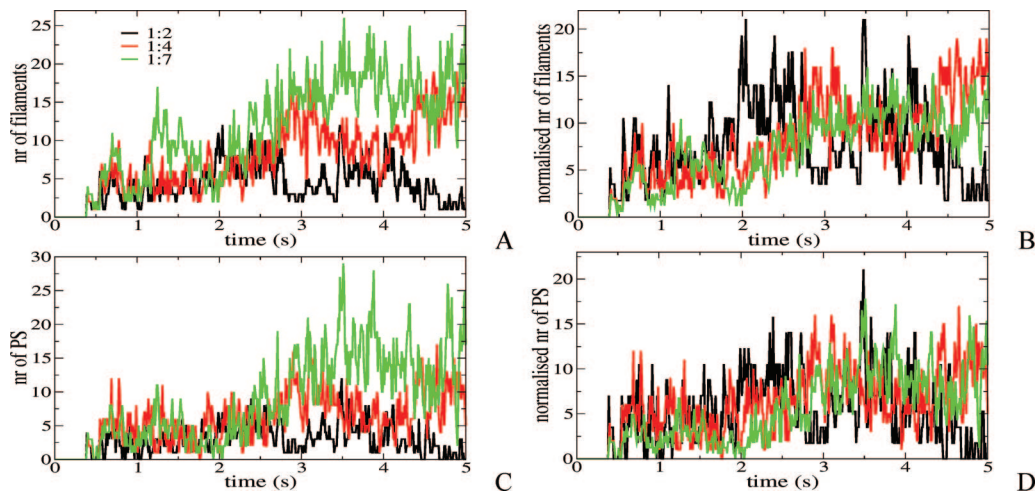
Figure 14A and 14B shows the wave pattern and scroll wave filaments for an episode of fibrillation when conductance of the fast sodium current is increased by a factor of 3 (parameter setting increased excitability in the Table). We can see that wave pattern complexity and number of filaments are somewhat larger than for the standard parameter setting (compare with Figures 3 and 9A). Figure 14C shows the time dynamics of the number of filaments and epicardially manifested rotors driving VF. After an initial transient, filament numbers approach an average of 12, and PS numbers an average of 8. Compared with Figures 8A and 9B, we can see that increasing GN a by a factor of 3 has no significant effect on the number of rotors driving VF. Figure 14D shows the ECG of this episode of VF, which has a dominant frequency of 5.2Hz.

**Dependence on APD Restitution, Maximum Slope**

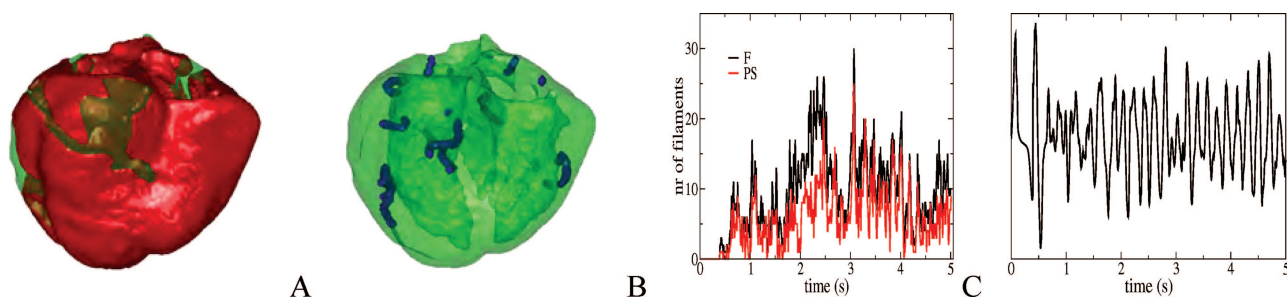
Maximum slope of the APD restitution curve has been found to differ between individuals and within individuals<sup>45</sup> and can clearly differ between species. Therefore, we investigated the effect of increasing restitution slope on VF complexity.

Figure 15A shows 2 APD restitution curves, 1 for the standard parameter setting used thus far and 1 for an alternative parameter setting that results in a higher maximum APD (386 versus 329 ms), a similar minimum APD (100 versus 110 ms), and a significantly higher maximum restitution slope (2.8 versus 1.8) (see the Table for parameter settings).

Figure 15B and 15C shows snapshots of wave patterns and scroll wave filaments arising after spiral breakup for the alternative parameter setting. Wave patterns appear more complex and filament numbers are larger than for the standard parameter setting (compare with Figures 3 and 9A). Figure 15D shows the number of filaments and epicardially manifested PS as a function of time. We can see that a steeper restitution slope leads to a 2- to 2.5-fold higher number of total rotors (average 24) and epicardial rotors (average 16) (compare with Figures 8A and 9B). Figure 15E shows the ECG of this simulated episode of VF, which has a dominant frequency of 4.8 Hz, comparable to that of the standard parameter setting.



**Figure 13.** A, Number (nr) of filaments as a function of time during VF for the different anisotropy ratios. B, Normalized number of filaments for the 3 different anisotropies. C, Number of epicardial PSs as a function of time for the 3 different anisotropy ratios. D, Normalized number of PSs for the 3 different anisotropies. Normalization is done relative to the effective ventricular volume for an anisotropy ratio of 1:4. Ratio between effective volumes for the different anisotropies than is 0.57:1:1.63 for the anisotropies 1:2, 1:4, and 1:7, respectively.



**Figure 14.** Effect of excitability. A, Wave pattern arising after scroll wave breakup for a scroll wave initialized in the anterior ventricular wall and a parameter setting with a factor 3 times higher sodium current conductance. B, Scroll wave filaments underlying the wave pattern in A. C, Number (nr) of filaments and epicardial PSs as a function of time for this episode of VF. D, Electrogram of the first 5 seconds of activity showing irregular VF-like dynamics.

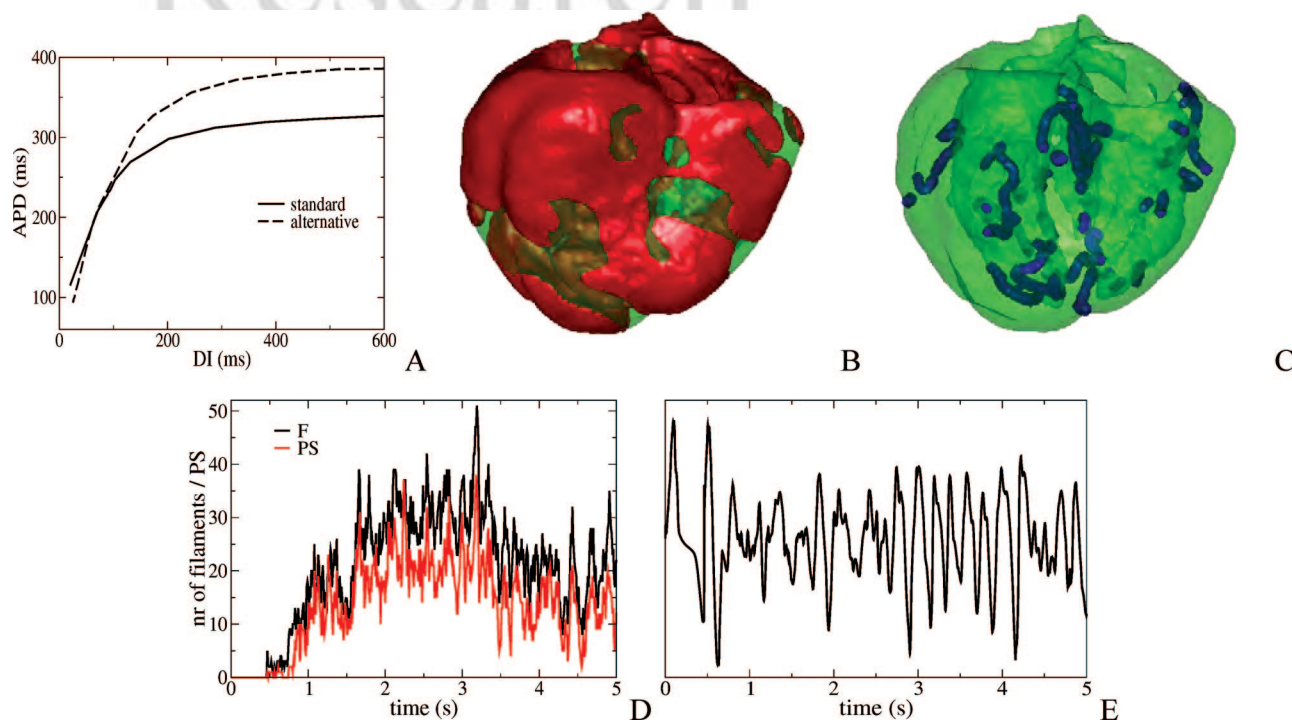
### Dependence on APD Restitution, Minimum APD

Another electrophysiological characteristic that may be subject to variation is minimum APD. Minimum APD is the shortest APD that can be reached during restitution protocols and fibrillation and is found to vary significantly between human and animal hearts (compare, for example, with previous reports<sup>23–25</sup>).

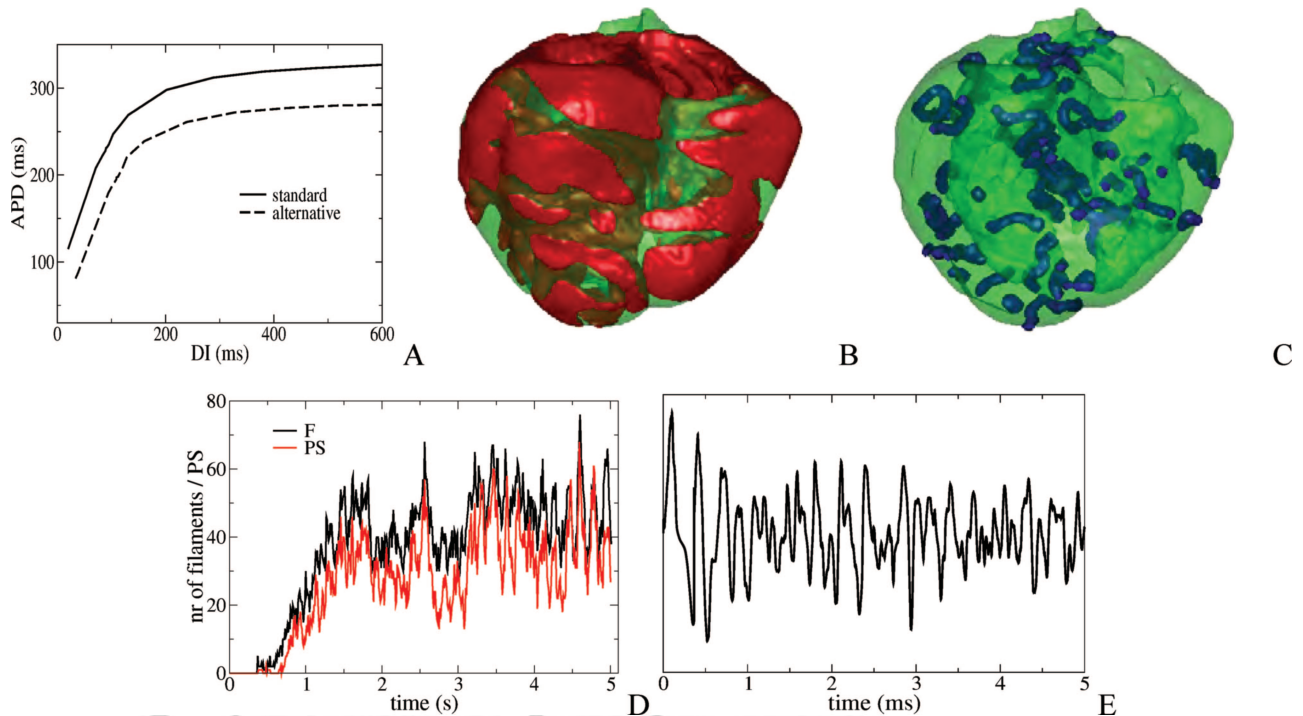
Figure 16A shows APD restitution curves for the standard parameter setting used thus far and for an alternative setting that results in a lower maximum APD (280 versus 329 ms), lower minimum APD (77 versus 110 ms), and similar maximum restitution slope (1.8) (see the Table for parameter settings).

Figure 16B and 16C shows snapshots of the wave pattern and scroll wave filaments arising after spiral breakup for the

alternative parameter setting. We can see that the wave pattern consists of more and smaller waves (compare with Figure 3) and is organized by a larger number of filaments (compare with Figure 9A) than for the standard parameter settings. In Figure 16D, we show the time dynamics of the number of rotors (filaments) and number of epicardially manifested rotors (PSs). We can see that after an initial increase, rotor numbers approach an average of 45 and PS numbers approach an average of 35, which is a factor of 4 to 5 higher than for the standard parameter setting (compare with Figures 8A and 9B). Figure 16E shows the ECG of this simulated episode of VF. We can see that the ECG is more irregular than for the standard parameter setting (compare with Figure 3D). The ECG has a dominant frequency of 6.7



**Figure 15.** Effect of maximum restitution slope. A, Restitution curves obtained using a dynamic restitution protocol showing the dependence of APD on DI for 2 different parameter settings. The standard parameter setting is that used throughout this article. The alternative setting is a modification of this standard setting, resulting in a steeper maximum restitution slope of 2.8 (see the Table for steeper restitution parameter setting). B, Snapshot of wave pattern arising after scroll wave fragmentation for the alternative parameter setting with steeper maximum restitution slope. C, Scroll wave filaments underlying the wave pattern in A. D, Number (nr) of filaments and epicardial PSs driving this episode of VF as a function of time. E, Electrogram of the first 5 seconds of activity showing irregular VF-like dynamics.



**Figure 16.** Effect of minimum APD. A, Restitution curves obtained using a dynamic restitution protocol showing the dependence of APD on DI for 2 different parameter settings. The standard parameter setting is that used throughout this article. The alternative setting is a modification of this standard setting, resulting in a lower minimum APD (see the Table for lower minimum APD parameter setting). B, Wave pattern arising after scroll wave fragmentation for the alternative parameter setting with lower minimum APD. C, Scroll wave filaments underlying the wave pattern in A. D, Number of filaments and epicardial PSs as a function of time for this episode of VF. E, Electrogram showing very irregular VF-like dynamics.

Hz, which is significantly higher than the frequencies found for the standard parameter setting.

We thus find that of the different factors studied, minimum APD has the largest influence on the number of rotors underlying VF.

### Discussion

Our understanding of VF in the human heart is still largely based on experimental studies using animal hearts. These studies have shown that the turbulent excitation pattern typical of VF is organized by multiple reentrant sources. Furthermore, these studies suggest that the number of rotors underlying VF increases with heart size. In the pig and dog heart, which have a size comparable to that of the human heart, VF is organized by approximately 50 reentrant sources.

Recent clinical measurements reporting a few large wavefronts and a small number of epicardial PSs<sup>12,13,18</sup> suggest that VF in the human heart could be much more organized than VF in large animal hearts. However, clinical and experimental measurements of VF are only made on the surface of the heart, leaving the possibility of larger numbers of rotors present inside the ventricular mass.

In this study, we used our detailed human ventricular model to study the wave organization during VF. Our model incorporates a detailed description of human ventricular anatomy, fiber direction anisotropy, and the electrophysiological behavior of human ventricular cells. We validated our model by simulating a normal ventricular activation sequence and comparing this with the classic data by Durrer et al.<sup>35</sup> We

then simulated VF by using a S1S2 protocol to initiate a spiral wave in the ventricles. We used a parameter setting that corresponds to a steep APD restitution curve (maximum slope 1.8) and results in breakup of the initial spiral wave and VF-like dynamics.

First, we performed an extensive comparison of our VF simulations with the clinical data from Nanthakumar et al<sup>12</sup> and Nash et al.<sup>13</sup> We showed that our simulated episodes of VF agree qualitatively with clinical VF in terms of ECG morphology and frequency, type and repeatability of surface wave patterns, and number of epicardially observable rotors. Following this, we studied the full 3D organization of simulated human VF. We illustrated how observing only (part of) the epicardial surface rather than the entire ventricular mass leads to an underestimation of the occurrence of reentry during VF. We found that the total number of rotors present during fibrillation lies at approximately 10 and is a factor of 1.3 to 1.4 higher than the number of epicardially manifested rotors.

We analyzed the history of filaments during episodes of VF, how they arise through birth and bifurcation events and disappear through death and amalgamation events, and the length of their lifespans. Similar to experimental observations on epicardially manifested rotors in animal hearts,<sup>37,38,43,46</sup> we found that most rotors are very short lived, whereas only one or a few long-lived rotors are present during a single episode of VF. We have shown that these longer-lived rotors are at the core of large clusters of filaments that all have arisen from the same initial filament through bifurcation events.

Our results indicate that human VF is indeed organized by a much smaller number of rotors than VF in animal hearts of comparable size. This finding implies that the spatial complexity of VF does not simply increase with heart size, as has been previously assumed, but that other factors need to be considered as well.

Why does VF in the human heart have a much simpler organization than VF in the dog and pig heart? To answer this question, we investigated the influence of a number of electrophysiological properties of cardiac tissue that may vary between human and animal hearts. Characteristics that were considered were tissue anisotropy ratio, tissue excitability, maximum APD restitution slope, and minimum APD. We found that VF wave pattern complexity and number of rotors were dependent on all factors studied. An increase in anisotropy ratio, excitability, and restitution slope and a decrease in minimum APD all led to more complex wave patterns and higher rotor numbers. For tissue anisotropy, the increase in rotor numbers could be explained by the increase in effective tissue mass. For tissue excitability and restitution slope, the increased wave pattern complexity probably resulted from an increase in the dynamical instability, leading to wave break formation. For minimum APD, the higher number of rotors was most likely caused by a shorter wave length, allowing a larger number of rotors to fit in the same tissue size.

We found that anisotropy ratio, excitability and restitution slope, when varied within the physiological range, could only account for a maximum increase of a factor of around 2 in rotor numbers. Decreasing minimum APD resulted in a factor of 5 more rotors and a significantly higher VF frequency, similar to rotor numbers and VF frequencies found in pig and dog hearts.<sup>5,6,14,15</sup> Interestingly, minimum APD in the pig and dog heart is significantly lower than in the human heart (140 to 200 ms for human,<sup>23</sup> 70 to 110 ms for dog,<sup>25</sup> and 90 to 110 ms<sup>24</sup> for pig). Therefore, we propose that it is the difference in minimum APD that causes the difference in spatial complexity, number of rotors, and frequency between human VF and dog and pig VF.

Our findings may have important consequences for the treatment and prevention of human VF. For example, in simulation studies, VF that is driven by a smaller number of rotors requires less energy for successful defibrillation.<sup>8,9</sup> Likewise, drugs aimed at increasing wave length or meander of reentrant sources to decrease the number of sources could be more promising to treat human VF than would be expected based on dog and pig heart experiments. Furthermore, our results suggest that minimum APD is an important determinant of VF wave pattern complexity. Increasing minimum APD leads to less reentrant sources and more coherent wave patterns. Minimum APD may thus be a potential new target for pharmacological interventions.

### Limitations

Although our simulation model incorporates a detailed description of human ventricular anatomy, fiber direction anisotropy, and cellular electrophysiology, it does not include all characteristics of human ventricular anatomy and function.

### Laminar Sheets

Cardiac muscle fibers are organized into laminar tissue sheets separated by connective tissue. As a consequence, conductivity transversal to fibers but within sheets is faster than conductivity transversal to both the fibers and tissue sheets (orthotropic anisotropy).<sup>47–49</sup> In our current model, these 2 transversal conductivities are assumed to be equal. The effect of orthotropic anisotropy on human VF organization thus remains an important topic for future research.

We feel that adequate incorporation of laminar sheets into cardiac models is not a trivial subject. Before one can do this, 2 important issues need to be addressed. (1) Is a continuous description of cardiac tissue suited for describing sheet structure, considering that sheets are separated by discrete nonconducting cleavage planes and, as was recently shown, that orientation of the cleavage planes is not uniquely defined by transmural location<sup>50</sup>? (2) How should we describe the laminar structure of the heart in a general (nonindividual specific) sense considering the reported variation among individual hearts of the same species<sup>50</sup>? Some important initial steps in solving these issues were taken in a report by Hooks et al,<sup>49</sup> in which a continuous versus discrete approach for modeling laminar structure were compared. However, this study was restricted to small rectangular tissue blocks, and the model simulation results were not compared with experimental wave propagation data.

We therefore think that the appropriate implementation of laminar sheet structure in cardiac models and an analysis of their possible effects on wave propagation during VF should be the subject of a separate study, results of which should be compared with the results of our present simulations.

### Heterogeneity

The current ventricular model consists of identical cells. However, in human and animal hearts, different types of electrophysiological heterogeneities have been reported, such as the base–apex gradient, the transmural epicardial–endocardial gradient, and the left–right ventricular gradient.<sup>51–54</sup> Modeling studies have shown that transmural electrophysiological gradients may enhance spiral wave breakup,<sup>55</sup> whereas planar gradients may enhance spiral wave drift.<sup>56</sup> Thus, heterogeneities may play a role in the initiation of VF. It remains to be investigated whether the presence of heterogeneity affects the number of re-entrant sources driving VF.

### Purkinje System

The ventricular model used in this study does not include a Purkinje system. However, clinical and simulation studies suggest that the Purkinje network may play an important role in arrhythmogenesis, both as a source of premature ectopic activations<sup>57</sup> and by offering extra routes for the propagating excitation wave.<sup>58,59</sup> Whether the presence of the Purkinje system also influences the number and dynamics of reentrant sources driving VF still needs to be investigated.

### Disease State

VF occurs predominantly in hearts that are abnormal, anatomically, electrophysiologically, or both. However, our human ventricular model represents a normal healthy human heart. The particular disease or condition of a patient, for

example, ischemic heart disease, cardiomyopathy, heart failure, Brugada syndrome, or long or short QT syndrome, may affect both the mechanism by which VF arises and the spatiotemporal complexity of VF.

Note that despite these limitations, we find very similar ECG morphology, ECG frequency, surface activation patterns, and number of epicardial PSs during simulated VF as compared with clinically recorded VF.

### Acknowledgments

We are grateful to Dr P. A. Helm and Dr R. L. Winslow at the Center for Cardiovascular Bioinformatics and Modeling of The Johns Hopkins University and Dr. E. R. McVeigh at the National Institutes of Health for providing the adult human heart DTMRI fiber direction data. We thank Dr P. S. Jouk and Dr Y. Usson from the Department of Genetics, Grenoble Teaching Hospital, Grenoble, France, and from the Equipe Reconnaissance des Formes et Microscopie Quantitative, Laboratoire TIMC, Grenoble, France, for providing the infant human heart microscopy fiber direction data. We thank Dr R. H. Clayton for helpful suggestions regarding this manuscript and to R. H. Kelderma for help with the construction of the filament ancestry figures.

### Sources of Funding

K.H.W.J.T.T. was supported by the Research Council for Physical Sciences of the Netherlands Organization for Scientific Research.

### Disclosures

None.

### References

1. Davidenko JM, Pertsov AM, Salomonsz R, Baxter W, Jalife J. Stationary and drifting spiral waves of excitation in isolated cardiac muscle. *Nature*. 1992;355:349–351.
2. Gray RA, Pertsov AM, Jalife J. Spatial and temporal organization during cardiac fibrillation. *Nature*. 1998;392:75–78.
3. Witkowski FX, Leon LJ, Penkoske PA, Giles WR, Spano ML, Ditto WL, Winfree AT. Spatiotemporal evolution of ventricular fibrillation. *Nature*. 1998;392:78–82.
4. Moreno J, Zaitsev AV, Warren M, Berenfeld O, Kalifa J, Lucca E, Mironov S, Guha P, Jalife J. Effect of remodelling, stretch and ischaemia on ventricular fibrillation frequency and dynamics in a heart failure model. *Cardiovasc Res*. 2005;65:158–166.
5. Huang J, Rogers JM, Killingsworth CR, Sing KP, Smith WM, Ideker RE. Evolution of activation patterns during long-duration ventricular fibrillation in dogs. *Am J Physiol Heart Circ Physiol*. 2004;101:H1139–H11200.
6. Valderrabano M, Chen P, Lin SF. Spatial distribution of phase singularities in ventricular fibrillation. *Circulation*. 2003;108:354–359.
7. Jalife J, Gray R. Drifting vortices of electrical waves underlie ventricular fibrillation in the rabbit heart. *Acta Physiol Scand*. 1996;157:123–131.
8. Plank G, Leon LJ, Kimber S, Vigmond EJ. Defibrillation depends on conductivity fluctuations and the degree of disorganization in reentry patterns. *J Cardiovasc Electrophysiol*. 2005;16:205–216.
9. Hillebrenner MG, Eason JC, Trayanova N. A Mechanistic inquiry into decrease in probability of defibrillation success with increase in complexity of preshock reentrant activity. *Am J Physiol Heart Circ Physiol*. 2004;286:H909–H917.
10. Panfilov AV. Is heart size a factor in ventricular fibrillation? Or how close are rabbit and human hearts? *Heart Rhythm*. 2006;3:862–864.
11. Clayton RH, Murray A, Campbell RW. Objective features of the surface electrocardiogram during ventricular tachyarrhythmias. *Eur Heart J*. 1995;16:1115–1119.
12. Nanthakumar K, Walcott GP, Melnick S, Rogers JM, Kay MW, Smith WM, Ideker RE, Holman W. Epicardial organization of human ventricular fibrillation. *Heart Rhythm*. 2004;1:14–23.
13. Nash MP, Mourad A, Clayton RH, Sutton PM, Bradley CP, Hayward M, Paterson DJ, Taggart P. Evidence for multiple mechanisms in human ventricular fibrillation. *Circulation*. 2006;114:536–542.
14. Newton J, Smith W, Ideker RE. Estimated global transmural distribution of activation rate and conduction block during porcine and canine ventricular fibrillation. *Circ Res*. 2004;94:836–842.
15. Nanthakumar K, Huang J, Rogers JM, Johnson P, Newton JC, Walcott GP, Justice RK, Rollings DL, Smith WM, Ideker RE. Regional differences in ventricular fibrillation in the open-chest porcine left ventricle. *Circ Res*. 2002;91:733–740.
16. Mandapati R, Asano Y, Baxter WT, Gray R, Davidenko J, Jalife J. Quantification of effects of global ischemia on dynamics of ventricular fibrillation in isolated rabbit heart. *Circulation*. 1998;98:1688–1696.
17. Zaitsev AV, Guha PK, Sarmast F, Kolli A, Berenfeld O, Pertsov AM, de Groot JR, Coronel R, Jalife J. Wavebreak formation during ventricular fibrillation in the isolated, regionally ischemic pig heart. *Circ Res*. 2003;86:546–553.
18. Walcott GP, Kay GN, Plumb VJ, Smith WM, Rogers JM, Epstein AE, Ideker RE. Endocardial wave front organization during ventricular fibrillation in humans. *J Am Coll Cardiol*. 2002;39:109–115.
19. Masse S, Downar E, Chauhan VS, Sevaptisid E, Nanthakumar K. Ventricular fibrillation in myopathic human hearts: mechanistic insights from in-vivo global endocardial and epicardial mapping. *Am J Physiol Heart Circ Physiol*. In press.
20. Ten Tusscher KHWJ, Noble D, Noble PJ, Panfilov AV. A model for human ventricular tissue. *Am J Physiol Heart Circ Physiol*. 2004;286:H1573–H1589.
21. Ten Tusscher KHWJ, Panfilov AV. Alternans and spiral breakup in a human ventricular tissue model. *Am J Physiol Heart Circ Physiol*. 2006;291:H1088–H1100.
22. Hren R. *A Realistic Model of the Human Ventricular Myocardium: Application to the Study of Ectopic Activation*. PhD Dissertation. Halifax, Nova Scotia, Canada: Dalhousie University; 1996.
23. Taggart P, Sutton P, Chalabi Z, Boyett MR, Simon R, Elliott D, Gill JS. Effect of adrenergic stimulation on action potential duration restitution in humans. *Circulation*. 2003;107:285–289.
24. Huang J, Zhou X, Smith WM, Ideker RE. Restitution properties during ventricular fibrillation in the in situ swine heart. *Circulation*. 2004;16:3161–3167.
25. Koller ML, Riccio ML, Gilmour RF Jr. Dynamic restitution of action potential duration during electrical alternans and ventricular fibrillation. *Am J Physiol Heart Circ Physiol*. 1998;275:H1635–H1642.
26. Keener J, Sneyd J. *Mathematical Physiology*. New York: Springer-Verlag; 1998.
27. Streeter DD Jr. Gross morphology and fiber geometry of the heart. In: Berne RM, Sperelakis N, eds. *Handbook of Physiology, Section 2: The Cardiovascular System, Volume 1: The Heart*. Bethesda, Md: American Physiology Society; 1979:61–112.
28. Nielsen PMF, LeGrice IJ, Smaill BH, Hunter PJ. A mathematical model of the geometry and fibrous structure of the heart. *Am J Physiol Heart Circ Physiol*. 1991;260:H1365–H1378.
29. Streeter DD Jr, Spotnitz MM, Patel DP, Ross J, Sonnenblick EH. Fiber orientation in the canine left ventricle during diastole and systole. *Circ Res*. 1969;24:339–347.
30. Scollan DF, Holmes A, Zhang J, Winslow RL. Reconstruction of cardiac ventricular geometry and fiber orientation using magnetic resonance imaging. *Ann Biomed Eng*. 2000;28:934–944.
31. Helm PA, Tseng H, Younes L, McVeigh ER, Winslow RL. Ex vivo 3D diffusion tensor imaging and quantification of cardiac laminar structure. *Magn Reson Med*. 2005;54:850–859.
32. Jouk PS, Usson Y, Michalowicz G, Grossi L. Three-dimensional cartography of the pattern of the myofibres in the second trimester fetal human heart. *Anat Embryol*. 2000;202:103–118.
33. Jouk PS, Mourad A, Milisic V, Michalowicz G, Raoult A, Caillierie D, Usson Y. Analysis of the fiber architecture of the heart by quantitative polarized light microscopy, accuracy, limitations and contribution to the study of the fiber architecture of the ventricles during fetal and neonatal life. *Eur J Cardiothorac Surg*. 2007;31:916–922.
34. Taggart P, Sutton PMI, Ophof T, Coronel R, Trimlett R, Pugsley W, Kallis P. Inhomogeneous transmural conduction during early ischemia in patients with coronary artery disease. *J Mol Cell Cardiol*. 2000;32:621–639.
35. Durrer D, Van Dam RT, Freud GE, Janse MJ, Meijler FL, Arzbacher RC. Total excitation of the isolated human heart. *Circulation*. 1970;41:899–912.
36. Plonsey R, Barr R. *Bioelectricity*. New York: Plenum Publishing Corp; 1989.

37. Kay MW, Walcott GP, Gladden JD, Melnick SB, Rogers JM. Lifetimes of epicardial rotors in panoramic optical maps of fibrillating swine ventricles. *Am J Physiol Heart Circ Physiol*. 2006;291:H1935–H1941.
38. Rogers JM, Huang J, Smith WM, Ideker RE. Incidence, evolution, and spatial distribution of functional reentry during ventricular fibrillation in pigs. *Circ Res*. 1999;84:945–954.
39. Rogers JM. Combined phase singularity and wavefront analysis for optical maps of ventricular fibrillation. *IEEE Trans Biomed Eng*. 2004;51:56–65.
40. Clayton RH, Holden AV. A method to quantify the dynamics and complexity of re-entry in computational models of ventricular fibrillation. *Phys Med Biol*. 2002;47:225–238.
41. Clayton RH, Zhuchkova EA, Panfilov AV. Phase singularities and filaments: simplifying complexity in computational models of ventricular fibrillation. *Prog Biophys Mol Biol*. 2006;90:378–398.
42. Fenton F, Karma A. Vortex dynamics in three-dimensional continuous myocardium with fiber rotation: filament instability and fibrillation. *Chaos*. 1998;8:20–47.
43. Valderrabano M, Lee MH, Ohara T, Lai AC, Fishbein MC, Lin SF, Karagueuzian HS, Chen PS. Dynamics of intramural and transmural reentry during ventricular fibrillation in isolated swine ventricles. *Circ Res*. 2001;88:839–848.
44. Clayton RH, Holden AV. Filament behaviour in a computational model of ventricular fibrillation in the canine heart. *IEEE Trans Biom Eng*. 2004;51:28–34.
45. Nash MP, Bradley CP, Sutton PM, Clayton RH, Kallis P, Hayward M, Paterson DJ, Taggart P. Whole heart action potential duration restitution properties in cardiac patients: a combined clinical and modeling study. *Exp Physiol*. 2006;91:339–354.
46. Rogers JM, Huang J, Melnick SB, Ideker RE. Sustained reentry in the left ventricle of fibrillating pig hearts. *Circ Res*. 2003;92:539–545.
47. LeGrice IJ, Smaill BH, Chai LZ, Edgar SG, Gavin JB, Hunter PJ. Laminar structure of the heart: ventricular myocyte arrangement and connective tissue architecture in the dog. *Am J Physiol Heart Circ Physiol*. 1995;269:H571–H582.
48. Hunter PJ, Smaill BH, Nielson PMF, LeGrice IJ. A mathematical model of cardiac anatomy. In: Panfilov AV and Holden AV, eds. *Computational Biology of the Heart*. Chichester, UK: Wiley; 1997:171–215.
49. Hooks DA, Tomlinson KA, Marsden SG, LeGrice IJ, Smaill BH, Pullan AJ, Hunter PJ. Cardiac microstructure: implications for electrical propagation and defibrillation in the heart. *Circ Res*. 2002;23:331–338.
50. Gilbert SH, Benson AP, Li P, Holden AV. Regional localisation of left ventricular sheet structure: integration with current models of cardiac fibre, sheet and band structure. *Eur J Cardiothorac Surg*. In press.
51. Burton FL, Cobbe SM. Dispersion of ventricular repolarization and refractory period. *Cardiovasc Res*. 2001;50:10–23.
52. Liu DW, Antzelevitch C. Characteristics of the delayed rectifier current ( $I_{Kr}$  and  $I_{Ks}$ ) in canine ventricular epicardial, midmyocardial, and endocardial myocytes. A weaker  $I_{Kr}$  contributes to the longer action potential of the M cell. *Circ Res*. 1995;76:351–365.
53. Zygmunt AC, Goodrow RJ, Antzelevitch C.  $I_{NaCa}$  contributes to electrical heterogeneity within the canine ventricle. *Am J Physiol Heart Circ Physiol*. 2000;278:H1671–H1678.
54. Samie FH, Berenfeld O, Anumonwo J, Mironov SF, Udassi S, Beaumont J, Taffet S, Pertsov AM, Jalife J. Rectification of the background potassium current: a determinant of rotor dynamics in ventricular fibrillation. *Circ Res*. 2001;89:1216–1223.
55. Clayton RH, Holden AV. Effect of regional differences in cardiac cellular electrophysiology on the stability of ventricular arrhythmias: a computational study. *Phys Med Biol*. 2003;48:95–111.
56. Ten Tusscher KHWJ, Panfilov AV. Reentry in heterogeneous cardiac tissue described by the Luo-Rudy ventricular action potential model. *Am J Physiol Heart Circ Physiol*. 2003;284:H542–H548.
57. Haïssaguerre M, Shah DC, Jais P, Shoda M, Kautzner J, Arentz T, Kalushe D, Kadish A, Griffith M, Gaita F, Yamane T, Garrigue S, Hocini M, Clémente J. Role of Purkinje conducting system in triggering of idiopathic ventricular fibrillation. *The Lancet*. 2002;359:677–678.
58. Ouyang F, Cappato R, Ernst S, Goya M, Volkmer M, Hebe J, Antz M, Vogtmann T, Schaumann A, Fotuhi P, Hoffman-Riem M, Kuck K. Electroanatomic substrate of idiopathic left ventricular tachycardia. Unidirectional block and macroreentry within the Purkinje network. *Circulation*. 2002;105:462–469.
59. Berenfeld O, Jalife J. Purkinje-muscle reentry as a mechanism of polymorphic ventricular arrhythmias in a 3-dimensional model of the ventricles. *Circ Res*. 1998;82:1063–1077.